中國機械工程學刊第三十九卷第五期第 459~469 頁(民國一百零七年)
Journal of the Chinese Society of Mechanical Engineers, Vol.39, No.5, pp 459~469 (2018)

A Method to Design a New Face Gear Drive That Has a Predesigned Fourth Order Function of Transmission Errors and Dimensionally Controllable Contact Ellipses

Cheng-Kang Lee

Keywords：fourth order function of transmission errors, face gear, tooth contact analysis, contact ellipses, principal curvatures and directions.

ABSTRACT

In terms of modern gear technology, the fourth order function of transmission errors (FOFTE) has been verified to be superior to a second order function of transmission errors (SOFTE). A FOFTE reduces noise levels and vibration. The motion curve that is formed by a FOFTE is smoother than the motion curve that is formed by a SOFTE. Transforming a SOFTE to a FOFTE has become the trend of research recently. This paper proposes a method to manufacture and design a new face gear drive that has a predesigned FOFTE and dimensionally controllable contact ellipses. Firstly, the position vectors, the unit normal vectors, the principal curvatures and the principal directions of the tooth faces of the new face gear drive are created using coordinate transformation theory, the theory of gearing and differential geometry. Secondly, the mathematical models for the tooth contact analysis and the mathematical model for the tangent slope of the function of transmission errors are developed to construct a system of eleven nonlinear equations. The system of nonlinear equations is used to compel the face gear drive to have the predesigned FOFTE. Finally, an optimization model is created using a full factorial design of experiment and Kriging interpolation to control the averages of the major and minor axes of the contact ellipses.

Paper Received June, 2018. Revised Sepfember, 2018. Accepted October, 2018. Author for Correspondence: Cheng-Kang Lee.

Associate Professor, Department of Industrial Engineering and Management, Cheng Shiu University, Kaohsiung, Taiwan 83347, ROC.

INTRODUCTION

Gear mechanisms are used in industry to transmit motion or torque between shafts. Theoretically, the gear ratio for a pair of circular gears is a constant. In reality, however, the gear ratio is not a constant due to the elastic deformation of materials, manufacturing errors, or assembly errors, so the function of transmission errors is no longer a horizontal zero line, in reality. If the function of transmission errors is linear in each period, it is referred to as a linear function of transmission errors. The motion curve that is formed by a linear function of transmission errors is not a continuous curve, which causes serious noise and vibration. To address this discontinuity in the motion curve, Litvin (1994) proposed a methodology that uses a predesigned second order function of transmission errors (SOFTE) to absorb the linear function of transmission errors. Using a SOFTE, the motion curve is transformed from discontinuous to continuous and the running noise and gear vibration are reduced. Based on Litvin's SOFTE methodology, many new gear drives have been proposed (Litvin and Lu, 1995; Seol and Litvin, 1996; Litvin and Kim, 1997; De Donno and Litvin, 1999; Litvin et al., 2000; Litvin et al., 2002a; Litvin et al., 2002b; Lee and Chen, 2004; Zanzi and Pedrero, 2005; Lee, 2015).

Stadtfeld and Gaiser (2000) in the Gleason Works reported that a fourth order function of transmission errors (FOFTE) is superior to a SOFTE. The motion curve formed by a FOFTE is smoother than the motion curve formed by a SOFTE. Less material must be removed for the tooth fillet for a FOFTE than a SOFTE. Therefore, a FOFTE reduces or eliminates gear noise and allows a strong tooth fillet. Wang and Fong (2006) proposed a methodology to synthesize tooth surfaces for a face-milling spiral bevel gear set that has a predetermined FOFTE. Lee (2009) proposed a manufacturing process for a cylindrical crowned gear drive that has a predesigned FOFTE. Peng et al. (2016) proposed a manufacturing process for the fabrication of ease-off surfaces for a face gear drive

that features controllable unloaded meshing and local bearing contact. Jiang and Fang (2015) proposed a design of tooth surface modifications to reduce vibration and noise for involute cylindrical gears that are provided with a controllable higher order polynomial function of transmission error. Li et al. (2017) proposed a function-oriented form-grinding approach to obtain excellent and stable contact performance of cylindrical gears by designing modification forms based on a predesigned controllable fourth-order transmission error function and error sensitivity evaluation.

The aim of this paper is to propose a method to manufacture and design a new face gear drive that has a predesigned FOFTE and dimensionally controllable contact ellipses. To compel the face gear drive to have the predesigned FOFTE, a system of eleven nonlinear equations with eleven unknown parameters are proposed. The eleven unknown parameters are determined using Newton's root finding method. To control the dimensions the contact ellipses, an optimization model is created based on a full factorial design of experiment and Kriging interpolation.

THE MATHEMATICAL MODEL FOR THE TOOTH FACE OF THE FACE GEAR

The position and unit normal vectors of the tooth face of the face gear

The face gear is generated using an involute shaper. The involute shaper is generated using an imaginary rack cutter. Figure 1 shows the profile L_r of the tooth face Σ_r of the imaginary rack cutter.

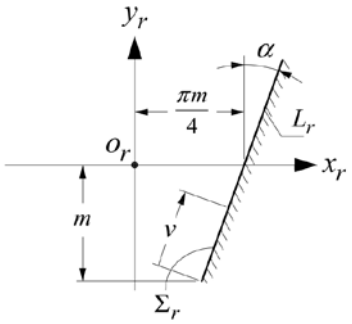

Fig. 1. Profile L_r of the tooth face Σ_r of the imaginary rack cutter

The coordinate system $S_r(o_r; x_r, y_r, z_r)$ is connected rigidly to Σ_r. The position and unit normal vectors of Σ_r represented in $S_r(o_r; x_r, y_r, z_r)$ are:

$$\begin{cases} \boldsymbol{r}_r(w,v) = \left[\dfrac{\pi m}{4} - m\tan\alpha + v\sin\alpha, -m + v\cos\alpha, w, 1\right]^T, \\ \boldsymbol{n}_r = \left[-\cos\alpha, \sin\alpha, 0\right]^T. \end{cases} \tag{1}$$

The tooth face Σ_r of the imaginary rack cutter is used to generate the tooth Σ_s of the involute shaper. Figure 2 shows the coordinate systems for the generation of Σ_s. The coordinate system $S_s(o_s; x_s, y_s, z_s)$ is connected rigidly to Σ_s. The linear displacement of Σ_r is $\rho_s\phi_s$. The angular displacement of Σ_s is ϕ_s. On Σ_s, the tooth face Σ_r forms a family of surfaces $\left\{\Sigma_r^{\phi s}\right\}$. The position and unit normal vectors of $\left\{\Sigma_r^{\phi s}\right\}$ represented in $S_s(o_s; x_s, y_s, z_s)$ are determined by

$$\begin{cases} \boldsymbol{r}_s^{(r)}(w,v,\phi_s) = \mathbf{M}_{sr}(\phi_s)\boldsymbol{r}_r(w,v), \\ \boldsymbol{n}_s^{(r)}(\phi_s) = \mathbf{L}_{sr}(\phi_s)\boldsymbol{n}_r. \end{cases} \tag{2}$$

The necessary condition for the existence of an envelope for the family of surfaces $\left\{\Sigma_r^{\phi s}\right\}$ is the following equation of meshing (Litvin, 1989):

$$\boldsymbol{n}_s^{(r)}(\phi_s)\cdot\left[\partial\boldsymbol{r}_s^{(r)}(w,v,\phi_s)/\partial\phi_s\right] = 0. \tag{3}$$

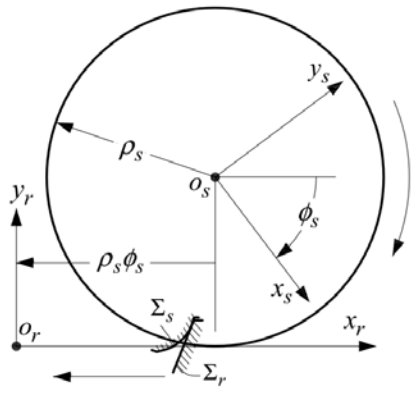

Fig. 2. Coordinate systems for the generation of Σ_s

The parameter v in Eq. (3) is represented by the explicit function ϕ_s, as follows:

$$v(\phi_s) = m\sec\alpha + (-\pi m/4 + \rho_s\phi_s)\sin\alpha. \tag{4}$$

The position and unit normal vectors of Σ_s represented in $S_s(o_s; x_s, y_s, z_s)$ are obtained as:

$$\begin{cases} \boldsymbol{r}_s(w,\phi_s) = \boldsymbol{r}_s^{(r)}\left(w, v(\phi_s), \phi_s\right), \\ \boldsymbol{n}_s(\phi_s) = \boldsymbol{n}_s^{(r)}(\phi_s). \end{cases} \tag{5}$$

The tooth face Σ_s of the involute shaper is used to generate the tooth face Σ_F of the face gear. Figure 3 shows the coordinate systems for the generation of Σ_F. The coordinate system $S_F(o_F; x_F, y_F, z_F)$ is

connected rigidly to Σ_F. The angular displacements of Σ_s and Σ_F are φ_s and φ_F, respectively.

$$\varphi_F = (N_s / N_F)\varphi_s = i_{sF}\varphi_s, \quad (6)$$

where N_s and N_F are the number of teeth on the involute shaper and on the face gear, respectively.

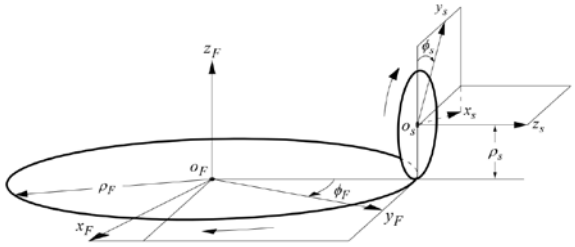

Fig. 3. Coordinate systems for the generation of Σ_F

On Σ_F, the tooth face Σ_s of the involute shaper forms a family of surfaces $\left\{\Sigma_s^{\varphi_s}\right\}$. The position and unit normal vectors of $\left\{\Sigma_s^{\varphi_s}\right\}$ represented in $S_F\left(o_F; x_F, y_F, z_F\right)$ are determined by

$$\begin{cases} \boldsymbol{r}_F^{(s)}(w,\phi_s,\varphi_s) = \mathbf{M}_{Fs}(\varphi_s)\boldsymbol{r}_s(w,\phi_s), \\ \boldsymbol{n}_F^{(s)}(\phi_s,\varphi_s) = \mathbf{L}_{Fs}(\varphi_s)\boldsymbol{n}_s(\phi_s). \end{cases} \quad (7)$$

The necessary condition for the existence of an envelope for $\left\{\Sigma_s^{\varphi_s}\right\}$ is the following equation of meshing (Litvin, 1989):

$$\boldsymbol{n}_F^{(s)}(\phi_s,\varphi_s)\cdot\left[\partial \boldsymbol{r}_F^{(s)}(w,\phi_s,\varphi_s)/\partial\varphi_s\right] = 0. \quad (8)$$

The parameter w in Eq. (8) is represented by the explicit function of ϕ_s and φ_s, as follows:

$$w(\phi_s,\varphi_s) = -\rho_F + \rho_s\cos\alpha\sec(\alpha - \phi_s + \varphi_s)/i_{sF}. \quad (9)$$

The position and unit normal vectors of Σ_F represented in $S_F\left(o_F; x_F, y_F, z_F\right)$ are obtained as:

$$\begin{cases} \boldsymbol{r}_F(\phi_s,\varphi_s) = \boldsymbol{r}_F^{(s)}\left(w(\phi_s,\varphi_s),\phi_s,\varphi_s\right), \\ \boldsymbol{n}_F(\phi_s,\varphi_s) = \boldsymbol{n}_F^{(s)}(\phi_s,\varphi_s). \end{cases} \quad (10)$$

The principal curvatures and directions of the tooth face of the face gear

The principal curvatures and directions of Σ_F can be determined using either differential geometry or kinematics (Litvin, 1989). Kinematics is more efficient than differential geometry because kinematics determines the principal curvatures and directions of Σ_F directly from the principal curvatures and directions of Σ_s and the kinematics parameters of Σ_s and Σ_F. The fundamental quantities of the first and second kinds of Σ_s are determined as follows:

$$\begin{cases} E_s = (\partial \boldsymbol{r}_s/\partial w)\cdot(\partial \boldsymbol{r}_s/\partial w) = 1, \\ F_s = (\partial \boldsymbol{r}_s/\partial w)\cdot(\partial \boldsymbol{r}_s/\partial \phi_s) = 0, \\ G_s = (\partial \boldsymbol{r}_s/\partial \phi_s)\cdot(\partial \boldsymbol{r}_s/\partial \phi_s), \\ L_s = \boldsymbol{n}_s\cdot(\partial^2 \boldsymbol{r}_s/\partial w^2) = 0, \\ M_s = \boldsymbol{n}_s\cdot(\partial^2 \boldsymbol{r}_s/\partial w\partial \phi_s) = 0, \\ N_s = \boldsymbol{n}_s\cdot(\partial^2 \boldsymbol{r}_s/\partial \phi_s{}^2). \end{cases} \quad (11)$$

The principal curvatures of Σ_s are determined by:

$$\kappa_{\mathrm{I}}^{(s)} = \frac{L_s}{E_s} = 0,\ \kappa_{\mathrm{II}}^{(s)} = \frac{N_s}{G_s}. \quad (12)$$

The principal directions of Σ_s represented in $S_s\left(o_s; x_s, y_s, z_s\right)$ are determined by:

$$\boldsymbol{e}_{\mathrm{I},s}^{(s)} = (\partial \boldsymbol{r}_s/\partial w)/\left|\partial \boldsymbol{r}_s/\partial w\right|,\ \boldsymbol{e}_{\mathrm{II},s}^{(s)} = \boldsymbol{n}_s \times \boldsymbol{e}_{\mathrm{I},s}^{(s)}. \quad (13)$$

The linear velocity of the origin o_s and the angular velocity of Σ_s represented in $S_s\left(o_s; x_s, y_s, z_s\right)$ are:

$$\boldsymbol{v}_s^{(s)} = \left[0,0,0\right]^T,\ \boldsymbol{\omega}_s^{(s)} = \left[0,0,-\omega_s\right]^T. \quad (14)$$

The linear velocity of the origin o_F and the angular velocity of Σ_F represented in $S_s\left(o_s; x_s, y_s, z_s\right)$ are:

$$\boldsymbol{v}_s^{(F)} = \left[0,0,0\right]^T,\ \boldsymbol{\omega}_s^{(F)} = \left[i_{sF}\omega_s\sin\varphi_s, -i_{sF}\omega_s\cos\varphi_s, 0\right]^T. \quad (15)$$

The position vector from the origin o_F to the origin o_s represented in $S_s\left(o_s; x_s, y_s, z_s\right)$ is:

$$(\overrightarrow{o_F o_s})_s = \left[-\rho_s\sin\varphi_s, \rho_s\cos\varphi_s, \rho_F\right]^T. \quad (16)$$

The relative linear and angular velocities of Σ_s with respect to Σ_F represented in $S_s\left(o_s; x_s, y_s, z_s\right)$ are determined by

$$\begin{cases} \boldsymbol{v}_s^{(sF)} = \boldsymbol{v}_s^{(s)} + \boldsymbol{\omega}_s^{(s)}\times\boldsymbol{r}_s - \boldsymbol{v}_s^{(F)} - \boldsymbol{\omega}_s^{(F)}\times\left[(\overrightarrow{o_F o_s})_s + \boldsymbol{r}_s\right], \\ \boldsymbol{\omega}_s^{(sF)} = \boldsymbol{\omega}_s^{(s)} - \boldsymbol{\omega}_s^{(F)}. \end{cases} \quad (17)$$

The principal curvatures and directions of Σ_F represented in $S_s\left(o_s; x_s, y_s, z_s\right)$ are determined using the following equations:

$$\begin{cases} \kappa_{\mathrm{I}}^{(F)} + \kappa_{\mathrm{II}}^{(F)} = \kappa_{\mathrm{I}}^{(s)} + \kappa_{\mathrm{II}}^{(s)} + \dfrac{s_1^2 + s_2^2}{s_3}, \\ \kappa_{\mathrm{I}}^{(F)} - \kappa_{\mathrm{II}}^{(F)} = \dfrac{s_1^2 - s_2^2 + s_3\left(\kappa_{\mathrm{I}}^{(s)} - \kappa_{\mathrm{II}}^{(s)}\right)}{s_3\cos 2\sigma^{(Fs)}}, \\ \boldsymbol{e}_{\mathrm{I},s}^{(F)} = \cos\sigma^{(Fs)}\boldsymbol{e}_{\mathrm{I},s}^{(s)} + \sin\sigma^{(Fs)}\boldsymbol{e}_{\mathrm{II},s}^{(s)}, \\ \boldsymbol{e}_{\mathrm{II},s}^{(F)} = -\sin\sigma^{(Fs)}\boldsymbol{e}_{\mathrm{I},s}^{(s)} + \cos\sigma^{(Fs)}\boldsymbol{e}_{\mathrm{II},s}^{(s)}, \\ \sigma^{(Fs)} = \dfrac{1}{2}\tan^{-1}\left(\dfrac{2s_1 s_2}{s_1^2 - s_2^2 + s_3\left(\kappa_{\mathrm{I}}^{(s)} - \kappa_{\mathrm{II}}^{(s)}\right)}\right), \end{cases} \quad (18)$$

where

$$\begin{cases} s_1 = -\kappa_{\mathrm{I}}^{(s)}(\boldsymbol{v}_s^{(sF)} \cdot \boldsymbol{e}_{\mathrm{I},s}^{(s)}) + (\boldsymbol{n}_s \times \boldsymbol{\omega}_s^{(sF)}) \cdot \boldsymbol{e}_{\mathrm{I},s}^{(s)}, \\ s_2 = -\kappa_{\mathrm{II}}^{(s)}(\boldsymbol{v}_s^{(sF)} \cdot \boldsymbol{e}_{\mathrm{II},s}^{(s)}) + (\boldsymbol{n}_s \times \boldsymbol{\omega}_s^{(sF)}) \cdot \boldsymbol{e}_{\mathrm{II},s}^{(s)}, \\ s_3 = \boldsymbol{v}_s^{(sF)} \cdot (\boldsymbol{n}_s \times \boldsymbol{\omega}_s^{(sF)}) - \kappa_{\mathrm{I}}^{(s)}(\boldsymbol{v}_s^{(sF)} \cdot \boldsymbol{e}_{\mathrm{I},s}^{(s)})^2 \\ -\kappa_{\mathrm{II}}^{(s)}(\boldsymbol{v}_s^{(sF)} \cdot \boldsymbol{e}_{\mathrm{II},s}^{(s)})^2 - \boldsymbol{n}_s \cdot \left[(\boldsymbol{\omega}_s^{(s)} + \boldsymbol{\omega}_s^{(F)}) \times (\boldsymbol{v}_s^{(F)} - \boldsymbol{v}_s^{(s)}) \right] \\ -\boldsymbol{n}_s \cdot \left\{ \boldsymbol{\omega}_s^{(s)} \times \left[\boldsymbol{\omega}_s^{(F)} \times \left(\boldsymbol{r}_s + (\overrightarrow{o_F o_s})_s \right) \right] - \boldsymbol{\omega}_s^{(F)} \times \left(\boldsymbol{\omega}_s^{(s)} \times \boldsymbol{r}_s \right) \right\}. \end{cases}$$

THE MATHEMATICAL MODEL FOR THE TOOTH FACE OF THE CROWNED PINION

The position and unit normal vectors of the tooth face of the crowned pinion

The crowned rack cutter is generated using a specially designed grinding wheel. The axial profile of the grinding wheel is designed using a fourth-degree polynomial curve. Figure 4 shows the axial profile L_g of the grinding wheel.

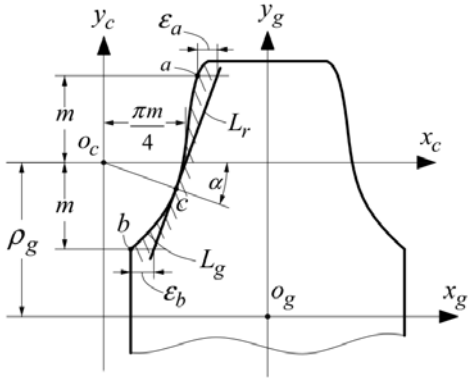

Fig. 4. Axial profile of the grinding wheel

The coordinate system $S_g\left(o_g; x_g, y_g, z_g\right)$ is connected rigidly to the grinding wheel. The mathematical model of L_g is represented in $S_g\left(o_g; x_g, y_g, z_g\right)$ by

$$\begin{bmatrix} x_g(u) \\ y_g(u) \end{bmatrix} = \begin{bmatrix} u \\ Au^4 + Bu^3 + Cu^2 + Du + E \end{bmatrix}. \tag{19}$$

The tangent slope of L_g is determined as follows:

$$y_g'(u) = 4Au^3 + 3Bu^2 + 2Cu + D, \tag{20}$$

The tangent slope of L_g at point c must be equal to $\cot\alpha$. The profile L_g must pass through three points, a, b and c. The tangent slope of L_g at point a must be equal to h_a. So, the five unknown coefficients of L_g are obtained as follows:

$$\begin{bmatrix} A \\ B \\ C \\ D \\ E \end{bmatrix} = \begin{bmatrix} a_{xg}^4 & a_{xg}^3 & a_{xg}^2 & a_{xg} & 1 \\ b_{xg}^4 & b_{xg}^3 & b_{xg}^2 & b_{xg} & 1 \\ c_{xg}^4 & c_{xg}^3 & c_{xg}^2 & c_{xg} & 1 \\ 4a_{xg}^3 & 3a_{xg}^2 & 2a_{xg} & 1 & 0 \\ 4c_{xg}^3 & 3c_{xg}^2 & 2c_{xg} & 1 & 0 \end{bmatrix}^{-1} \begin{bmatrix} a_{yg} \\ b_{yg} \\ c_{yg} \\ h_a \\ \cot\alpha \end{bmatrix}, \tag{21}$$

where

$$\begin{cases} a_{xg} = (-\pi m/4) + m\tan\alpha - \varepsilon_a, \\ a_{yg} = \rho_g + m, \\ b_{xg} = (-\pi m/4) - m\tan\alpha - \varepsilon_b, \\ b_{yg} = \rho_g - m, \\ c_{xg} = (-\pi m/2) + (\pi m/4)\cos^2\alpha, \\ c_{yg} = \rho_g - (\pi m/4)\cos\alpha\sin\alpha. \end{cases}$$

Rotating the axial profile L_g about the axis of revolution x_g yields the revolving surface Σ_g of the grinding wheel. The position and unit normal vectors of Σ_g represented in $S_g\left(o_g; x_g, y_g, z_g\right)$ are obtained as:

$$\begin{cases} \boldsymbol{r}_g(\theta, u) = \left[u, y_g(u)\cos\theta, y_g(u)\sin\theta, 1\right]^T, \\ \boldsymbol{n}_g(\theta, u) = \dfrac{1}{\sqrt{1 + y_g'(u)^2}}\left[-y_g'(u), \cos\theta, \sin\theta\right]^T. \end{cases} \tag{22}$$

The revolving surface Σ_g of the grinding wheel is used to generate the tooth face Σ_c of the crowned rack cutter. Figure 5 shows the coordinate systems for the generation of Σ_c.

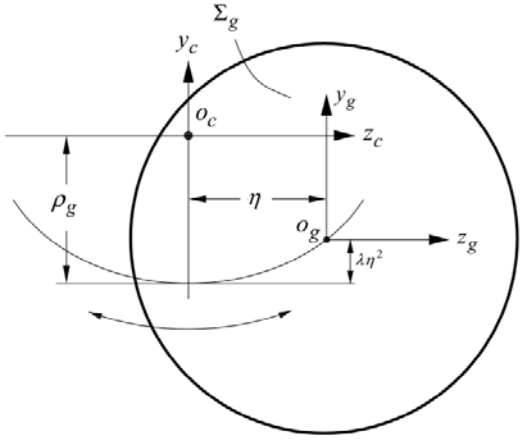

Fig. 5. Coordinate systems for the generation of Σ_c

The coordinate system $S_c\left(o_c; x_c, y_c, z_c\right)$ is connected rigidly to Σ_c. The revolving surface Σ_g has a parabolic motion with respect to Σ_c. On Σ_c, the revolving surface Σ_g forms a family of surfaces

$\{\Sigma_g^{\eta}\}$. The position vector of $\{\Sigma_g^{\eta}\}$ represented in $S_c(o_c; x_c, y_c, z_c)$ is determined by

$$\boldsymbol{r}_c^{(g)}(\theta,u,\eta) = \mathbf{M}_{cg}(\eta)\boldsymbol{r}_g(\theta,u), \tag{23}$$

The necessary condition for the existence of an envelope for $\{\Sigma_g^{\eta}\}$ is:

$$\eta(\theta) = \frac{-\tan\theta}{2\lambda}. \tag{24}$$

The position and unit normal vectors of Σ_c represented in $S_c(o_c; x_c, y_c, z_c)$ are obtained as:

$$\begin{cases} \boldsymbol{r}_c(\theta,u) = \boldsymbol{r}_c^{(g)}\left(\theta,u,\eta(\theta)\right), \\ \boldsymbol{n}_c(\theta,u) = \boldsymbol{n}_g(\theta,u). \end{cases} \tag{25}$$

The tooth Σ_c of the crowned rack cutter is used to generate the tooth face Σ_p of the crowned pinion. Figure 6 shows the coordinate systems for the generation of Σ_p. The coordinate system $S_p(o_p; x_p, y_p, z_p)$ is connected rigidly to the crowned pinion. The linear displacement of Σ_c is $\rho_p\phi_p$. The angular displacement of Σ_p is ϕ_p. On Σ_p, the tooth face Σ_c forms a family of surfaces $\{\Sigma_c^{\phi_p}\}$. The position and unit normal vectors of $\{\Sigma_c^{\phi_p}\}$ represented in $S_p(o_p; x_p, y_p, z_p)$ are determined by

$$\begin{cases} \boldsymbol{r}_p^{(c)}(\theta,u,\phi_p) = \mathbf{M}_{pc}(\phi_p)\boldsymbol{r}_c(\theta,u), \\ \boldsymbol{n}_p^{(c)}(\theta,u,\phi_p) = \mathbf{L}_{pc}(\phi_p)\boldsymbol{n}_c(\theta,u). \end{cases} \tag{26}$$

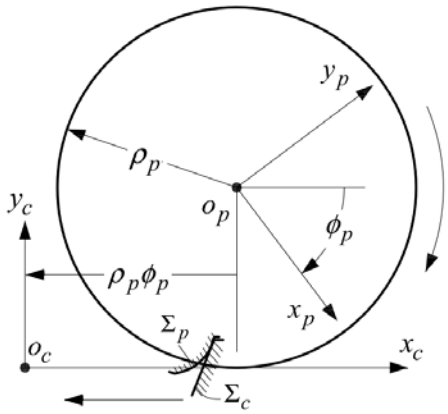

Fig. 6. Coordinate systems for the generation of Σ_p

The necessary condition for the existence of an envelope for $\{\Sigma_c^{\phi p}\}$ is the following equation of meshing:

$$\Omega(\theta,u,\phi_p) = \boldsymbol{n}_p^{(c)}(\theta,u,\phi_p)\cdot\left[\partial\boldsymbol{r}_p^{(c)}(\theta,u,\phi_p)/\partial\phi_p\right] = 0. \tag{27}$$

The parameter ϕ_p in Eq. (27) is represented by an explicit function of θ and u as follows:

$$\begin{aligned} \phi_p(\theta,u) &= \frac{(m\pi + 2u)}{2\rho_p} \\ &+ \frac{[4\lambda y_g(u) + (-4\lambda\rho_g + \tan^2\theta)\sec\theta]y_g'(u)}{4\lambda\rho_p}. \end{aligned} \tag{28}$$

The position and unit normal vectors of Σ_p represented in $S_p(o_p; x_p, y_p, z_p)$ are obtained as:

$$\begin{cases} \boldsymbol{r}_p(\theta,u) = \boldsymbol{r}_p^{(c)}\left(\theta,u,\phi_p(\theta,u)\right), \\ \boldsymbol{n}_p(\theta,u) = \boldsymbol{n}_p^{(c)}\left(\theta,u,\phi_p(\theta,u)\right). \end{cases} \tag{29}$$

The principal curvatures and directions of the tooth face of the crowned pinion

The principal curvatures and directions of Σ_p are also determined using kinematics. The fundamental quantities of the first and second kinds of Σ_c are determined as follows:

$$\begin{cases} E_c = (\partial\boldsymbol{r}_c/\partial\theta)\cdot(\partial\boldsymbol{r}_c/\partial\theta) = \dfrac{[\sec^3\theta - 2\lambda y_g(u)]^2}{4\lambda^2}, \\ F_c = (\partial\boldsymbol{r}_c/\partial\theta)\cdot(\partial\boldsymbol{r}_s/\partial u) = 0, \\ G_c = (\partial\boldsymbol{r}_c/\partial u)\cdot(\partial\boldsymbol{r}_c/\partial u) = 1 + y_g'(u)^2, \\ L_c = \boldsymbol{n}_c\cdot(\partial^2\boldsymbol{r}_c/\partial\theta^2) = \dfrac{\sec^3\theta - 2\lambda y_g(u)}{2\lambda\sqrt{1+y_g'(u)^2}}, \\ M_c = \boldsymbol{n}_c\cdot(\partial^2\boldsymbol{r}_c/\partial\theta\,\partial u) = 0, \\ N_c = \boldsymbol{n}_c\cdot(\partial^2\boldsymbol{r}_c/\partial u^2) = \dfrac{y_g''(u)}{\sqrt{1+y_g'(u)^2}}. \end{cases} \tag{30}$$

The principal curvatures of Σ_c are determined by

$$\kappa_{\mathrm{I}}^{(c)} = \frac{L_c}{E_c},\ \kappa_{\mathrm{II}}^{(c)} = \frac{N_c}{G_c}. \tag{31}$$

The principal directions of Σ_c represented in $S_c(o_c; x_c, y_c, z_c)$ are determined by

$$\boldsymbol{e}_{\mathrm{I},c}^{(c)} = (\partial\boldsymbol{r}_c/\partial\theta)/|\partial\boldsymbol{r}_c/\partial\theta|,\ \boldsymbol{e}_{\mathrm{II},c}^{(c)} = \boldsymbol{n}_c\times\boldsymbol{e}_{\mathrm{I},c}^{(c)}. \tag{32}$$

The velocity of the origin o_c and the angular velocity of Σ_c represented in $S_c(o_c; x_c, y_c, z_c)$ are:

$$\boldsymbol{v}_c^{(c)} = \left[-\rho_p\omega_p, 0, 0\right]^T,\ \boldsymbol{\omega}_c^{(c)} = [0,0,0]^T. \tag{33}$$

The velocity of the origin o_p and the angular velocity of Σ_p represented in $S_c(o_c; x_c, y_c, z_c)$ are:

$$\boldsymbol{v}_c^{(p)} = [0,0,0]^T,\ \boldsymbol{\omega}_c^{(p)} = \left[0,0,-\omega_p\right]^T. \tag{34}$$

The position vector from the origin o_p to the origin o_c represented in $S_c(o_c; x_c, y_c, z_c)$ is:

$$(\overrightarrow{o_p o_c})_c = \left[-\rho_p\phi_p, -\rho_p, 0\right]^T. \tag{35}$$

The relative linear and angular velocities of Σ_c with respect to Σ_p represented in $S_c\left(o_c;x_c,y_c,z_c\right)$ are determined by

$$\begin{cases}\boldsymbol{v}_c^{(cp)}=\boldsymbol{v}_c^{(c)}+\boldsymbol{\omega}_c^{(c)}\times\boldsymbol{r}_c-\boldsymbol{v}_c^{(p)}-\boldsymbol{\omega}_c^{(p)}\times\left[(\overrightarrow{o_po_c})_c+\boldsymbol{r}_c\right],\\ \boldsymbol{\omega}_c^{(cp)}=\boldsymbol{\omega}_c^{(c)}-\boldsymbol{\omega}_c^{(p)}.\end{cases} \tag{36}$$

The principal curvatures and directions of Σ_p represented in $S_c\left(o_c;x_c,y_c,z_c\right)$ are determined using the following equations:

$$\begin{cases}\kappa_{\mathrm{I}}^{(p)}+\kappa_{\mathrm{II}}^{(p)}=\kappa_{\mathrm{I}}^{(c)}+\kappa_{\mathrm{II}}^{(c)}+\dfrac{c_1^2+c_2^2}{c_3},\\ \kappa_{\mathrm{I}}^{(p)}-\kappa_{\mathrm{II}}^{(p)}=\dfrac{c_1^2-c_2^2+c_3(\kappa_{\mathrm{I}}^{(c)}-\kappa_{\mathrm{II}}^{(c)})}{c_3\cos 2\sigma^{(pc)}},\\ \boldsymbol{e}_{1,c}^{(p)}=\cos\sigma^{(pc)}\boldsymbol{e}_{1,c}^{(c)}+\sin\sigma^{(pc)}\boldsymbol{e}_{\mathrm{II},c}^{(c)},\\ \boldsymbol{e}_{\mathrm{II},c}^{(p)}=-\sin\sigma^{(pc)}\boldsymbol{e}_{1,c}^{(c)}+\cos\sigma^{(pc)}\boldsymbol{e}_{\mathrm{II},c}^{(c)},\\ \sigma^{(pc)}=\dfrac{1}{2}\tan^{-1}\left(\dfrac{2c_1c_2}{c_1^2-c_2^2+c_3(\kappa_{\mathrm{I}}^{(c)}-\kappa_{\mathrm{II}}^{(c)})}\right),\end{cases} \tag{37}$$

where

$$\begin{cases}c_1=-\kappa_{\mathrm{I}}^{(c)}(\boldsymbol{v}_c^{(cp)}\cdot\boldsymbol{e}_{1,c}^{(c)})+(\boldsymbol{n}_c\times\boldsymbol{\omega}_c^{(cp)})\cdot\boldsymbol{e}_{1,c}^{(c)},\\ c_2=-\kappa_{\mathrm{II}}^{(c)}(\boldsymbol{v}_c^{(cp)}\cdot\boldsymbol{e}_{\mathrm{II},c}^{(c)})+(\boldsymbol{n}_c\times\boldsymbol{\omega}_c^{(cp)})\cdot\boldsymbol{e}_{\mathrm{II},c}^{(c)},\\ c_3=\boldsymbol{v}_c^{(cp)}\cdot(\boldsymbol{n}_c\times\boldsymbol{\omega}_c^{(cp)})-\kappa_{\mathrm{I}}^{(c)}(\boldsymbol{v}_c^{(cp)}\cdot\boldsymbol{e}_{1,c}^{(c)})^2\\ -\kappa_{\mathrm{II}}^{(c)}(\boldsymbol{v}_c^{(cp)}\cdot\boldsymbol{e}_{\mathrm{II},c}^{(c)})^2-\boldsymbol{n}_c\cdot\left[(\boldsymbol{\omega}_c^{(c)}+\boldsymbol{\omega}_c^{(p)})\times(\boldsymbol{v}_c^{(p)}-\boldsymbol{v}_c^{(c)})\right]\\ -\boldsymbol{n}_c\cdot\left\{\boldsymbol{\omega}_c^{(c)}\times\left[\boldsymbol{\omega}_c^{(p)}\times\left(\boldsymbol{r}_c+(\overrightarrow{o_po_c})_c\right)\right]-\boldsymbol{\omega}_c^{(p)}\times\left(\boldsymbol{\omega}_c^{(c)}\times\boldsymbol{r}_c\right)\right\}.\end{cases}$$

THE MATHEMATICAL MODEL FOR TOOTH CONTACT ANALYSIS AND CONTACT ELLIPSE ANALYSIS

The condition of contact and the function of transmission errors

Tooth contact analysis (TCA) technology can be used to determine the contact paths on the tooth faces, the function of transmission errors and the contact ellipses (Litvin, 1994). Figure 7 shows the coordinate systems for performing TCA.

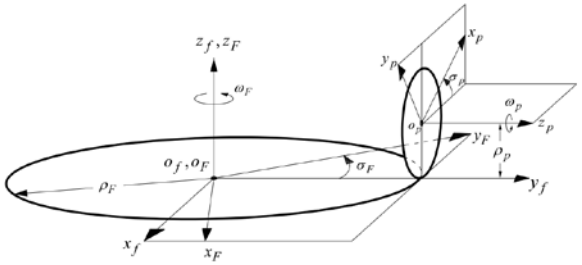

Fig. 7. Coordinate systems for performing tooth contact analysis

The coordinate system $S_f\left(o_f;x_f,y_f,z_f\right)$ is connected rigidly to the gear housing. The tooth face Σ_p of the crowned pinion is the driving face and the tooth face Σ_F of the face gear is the driven face. The respective angular displacements of Σ_p and Σ_F are σ_p and σ_F. The position and unit normal vectors of Σ_p represented in $S_f\left(o_f;x_f,y_f,z_f\right)$ are determined by

$$\begin{cases}\boldsymbol{r}_f^{(p)}(\theta,u,\sigma_p)=\mathbf{M}_{fp}(\sigma_p)\boldsymbol{r}_p(\theta,u),\\ \boldsymbol{n}_f^{(p)}(\theta,u,\sigma_p)=\mathbf{L}_{fp}(\sigma_p)\boldsymbol{n}_p(\theta,u),\end{cases} \tag{38}$$

The position and unit normal vectors of Σ_F represented in $S_f\left(o_f;x_f,y_f,z_f\right)$ are determined by

$$\begin{cases}\boldsymbol{r}_f^{(F)}(\phi_s,\varphi_s,\sigma_F)=\mathbf{M}_{fF}(\sigma_F)\boldsymbol{r}_F(\phi_s,\varphi_s),\\ \boldsymbol{n}_f^{(F)}(\phi_s,\varphi_s,\sigma_F)=\mathbf{L}_{fF}(\sigma_F)\boldsymbol{n}_F(\phi_s,\varphi_s),\end{cases} \tag{39}$$

The condition of contact is represented as:

$$\begin{cases}\boldsymbol{r}_f^{(F)}(\phi_s,\varphi_s,\sigma_F)-\boldsymbol{r}_f^{(p)}(\theta,u,\sigma_p)=\boldsymbol{0},\\ \boldsymbol{n}_f^{(F)}(\phi_s,\varphi_s,\sigma_F)-\boldsymbol{n}_f^{(p)}(\theta,u,\sigma_p)=\boldsymbol{0}.\end{cases} \tag{40}$$

There are five independent nonlinear algebraic scalar equations with six unknown parameters in Eq. (40). Using the theorem for the existence of an implicit function system, the five independent algebraic scalar equations are used to determine the following five implicit functions:

$$\{\theta(\sigma_p),u(\sigma_p),\phi_s(\sigma_p),\varphi_s(\sigma_p),\sigma_F(\sigma_p)\}. \tag{41}$$

The function of transmission errors is also represented by a function of σ_p as:

$$\Delta\sigma_F=\sigma_F(\sigma_p)-\left(N_p/N_F\right)\sigma_p. \tag{42}$$

The tangent slope of the function of transmission errors

To produce the predesigned FOFTE, it is necessary to control the slope of the function of transmission errors. Using calculus, the tangent slope of the function of transmission errors is:

$$h_\Delta=\sigma_F'(\sigma_p)-\left(N_p/N_F\right). \tag{43}$$

For any contact point, the inner product of $\boldsymbol{n}_f^{(p)}(\theta,u,\sigma_p)$ and $\boldsymbol{v}_f^{(pF)}(\theta,u,\sigma_p)$ is zero:

$$\boldsymbol{n}_f^{(p)}(\theta,u,\sigma_p)\cdot\boldsymbol{v}_f^{(pF)}(\theta,u,\sigma_p)=0. \tag{44}$$

The relative linear velocity $\boldsymbol{v}_f^{(pF)}(\theta,u,\sigma_p)$ is determined by:

$$\boldsymbol{v}_f^{(pF)}(\theta,u,\sigma_p)=\left(d\sigma_p/dt\right)\left[\boldsymbol{k}_f^{(p)}(\sigma_p)\times\boldsymbol{R}_f^{(p)}(\theta,u,\sigma_p)\right]$$
$$-\left(d\sigma_p/dt\right)\left[\sigma_F'(\sigma_p)\boldsymbol{k}_f^{(F)}(\sigma_F)\times\boldsymbol{R}_f^{(F)}(\phi_s,\varphi_s,\sigma_F)\right]. \tag{45}$$

Therefore, the tangent slope of the function of transmission errors is determined by:

$$h_{\Delta}(\theta,u,\sigma_p,\phi_s,\varphi_s,\sigma_F)=\sigma_F{}'(\sigma_p)-\left(N_p/N_F\right)$$
$$=\frac{\boldsymbol{n}_f^{(p)}(\theta,u,\sigma_p)\cdot\left[\boldsymbol{k}_f^{(p)}(\sigma_p)\times\boldsymbol{R}_f^{(p)}(\theta,u,\sigma_p)\right]}{\boldsymbol{n}_f^{(p)}(\theta,u,\sigma_p)\cdot\left[\boldsymbol{k}_f^{(F)}(\sigma_F)\times\boldsymbol{R}_f^{(F)}(\phi_s,\varphi_s,\sigma_F)\right]}-\left(N_p/N_F\right). \quad (46)$$

The major and minor axes and the direction of contact ellipses

Because of the elasticity of the materials, the theoretical contact point of the meshing tooth faces Σ_p and Σ_F is spread over a contact area. The projection of the contact area on the tangent plane is an elliptical area if Σ_p and Σ_F are approximated by their second order Taylor series expansions. The elliptical area is called a contact ellipse. The bearing contact is composed of a series of contact ellipses. The center of symmetry of the contact ellipse coincides with the theoretical contact point. The major axis $2a$, the minor axis $2b$ and the orientation of the contact ellipse are determined using the elastic approach δ of the meshing surfaces and the principal curvatures and directions of the meshing surfaces (Litvin, 1994). The meshing surfaces are the tooth face Σ_p of the crowned pinion and the tooth face Σ_F of the face gear. The angle that is measured counterclockwise from $\boldsymbol{e}_{\mathrm{I}}^{(F)}$ to $\boldsymbol{e}_{\mathrm{I}}^{(p)}$ is ψ and is determined using the following equations:

$$\begin{cases}\cos\psi=\boldsymbol{e}_{1,f}^{(p)}\cdot\boldsymbol{e}_{1,f}^{(F)}=\left(\mathbf{L}_{fp}\mathbf{L}_{pc}\boldsymbol{e}_{1,c}^{(p)}\right)\cdot\left(\mathbf{L}_{fF}\mathbf{L}_{Fs}\boldsymbol{e}_{1,s}^{(F)}\right),\\ \sin\psi=\boldsymbol{e}_{1,f}^{(p)}\cdot\boldsymbol{e}_{\mathrm{II},f}^{(F)}=\left(\mathbf{L}_{fp}\mathbf{L}_{pc}\boldsymbol{e}_{1,c}^{(p)}\right)\cdot\left(\mathbf{L}_{fF}\mathbf{L}_{Fs}\boldsymbol{e}_{\mathrm{II},s}^{(F)}\right).\end{cases} \quad (47)$$

The angle that is measured counterclockwise from $\boldsymbol{e}_{\mathrm{I}}^{(p)}$ to the direction τ is μ and is determined using the following equations:

$$\begin{cases}\cos 2\mu=\dfrac{g_1-g_2\cos 2\psi}{(g_1^2-2g_1g_2\cos 2\psi+g_2^2)^{1/2}},\\ \sin 2\mu=\dfrac{g_2\sin 2\psi}{(g_1^2-2g_1g_2\cos 2\psi+g_2^2)^{1/2}}.\end{cases} \quad (48)$$

The major and minor axes of the contact ellipse are determined using the following equations:

$$2a=2\left|\delta/T_1\right|^{1/2},\ 2b=2\left|\delta/T_2\right|^{1/2}, \quad (49)$$

where

$$\begin{cases}T_1=\dfrac{1}{4}\left[\kappa_{\Sigma}^{(p)}-\kappa_{\Sigma}^{(F)}-(g_1^2-2g_1g_2\cos 2\psi+g_2^2)^{1/2}\right],\\ T_2=\dfrac{1}{4}\left[\kappa_{\Sigma}^{(p)}-\kappa_{\Sigma}^{(F)}+(g_1^2-2g_1g_2\cos 2\psi+g_2^2)^{1/2}\right],\\ \kappa_{\Sigma}^{(p)}=\kappa_{\mathrm{I}}^{(p)}+\kappa_{\mathrm{II}}^{(p)},\ \kappa_{\Sigma}^{(F)}=\kappa_{\mathrm{I}}^{(F)}+\kappa_{\mathrm{II}}^{(F)},\\ g_1=\kappa_{\mathrm{I}}^{(p)}-\kappa_{\mathrm{II}}^{(p)},\ g_2=\kappa_{\mathrm{I}}^{(F)}-\kappa_{\mathrm{II}}^{(F)}.\end{cases}$$

PRODUCING THE PREDESIGNED FOURTH ORDER FUNCTION OF TRANSMISSION ERRORS

The proposed face gear drive can produce the predesigned FOFTE as long as the design parameters, ε_a, ε_b and h_a, of L_g are determined by the following method. Figure 8 shows the model of the predesigned FOFTE.

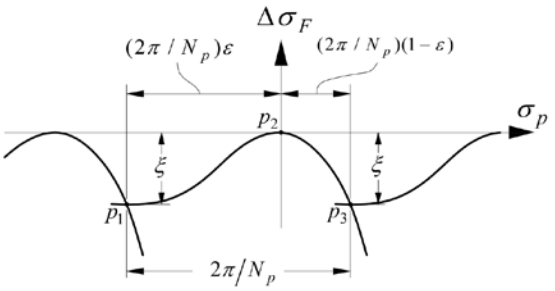

Fig. 8. Model of the predesigned FOFTE

The middle curve of the predesigned FOFTE is composed of two parts. The left part is from p_1 to p_2. The right part is from p_2 to p_3. The horizontal distance between p_1 and p_3 is $2\pi/N_p$. The slope of the FOFTE at p_1 is zero. For p_1, parameters θ, u, ϕ_s, φ_s, σ_p and σ_F are respectively replaced by θ_1, u_1, ϕ_{s1}, φ_{s1}, σ_{p1} and σ_{F1}, which are constrained by

$$\begin{cases}\boldsymbol{r}_f^{(F)}(\phi_{s1},\varphi_{s1},\sigma_{F1})-\boldsymbol{r}_f^{(p)}(\theta_1,u_1,\sigma_{p1})=\boldsymbol{0},\\ \boldsymbol{n}_f^{(F)}(\phi_{s1},\varphi_{s1},\sigma_{F1})-\boldsymbol{n}_f^{(p)}(\theta_1,u_1,\sigma_{p1})=\boldsymbol{0},\\ h_{\Delta}(\theta_1,u_1,\sigma_{p1},\phi_{s1},\varphi_{s1},\sigma_{F1})=0,\\ \sigma_{p1}=-\left(2\pi/N_p\right)\varepsilon,\\ \sigma_{F1}=-\xi-\left(N_p/N_F\right)\left(2\pi/N_p\right)\varepsilon.\end{cases} \quad (50)$$

For p_3, parameters θ, u, ϕ_s, φ_s, σ_p and σ_F are respectively replaced by θ_3, u_3, ϕ_{s3}, φ_{s3}, σ_{p3} and σ_{F3}, which are constrained by

$$\begin{cases}\boldsymbol{r}_f^{(F)}(\phi_{s3},\varphi_{s3},\sigma_{F3})-\boldsymbol{r}_f^{(p)}(\theta_3,u_3,\sigma_{p3})=\boldsymbol{0},\\ \boldsymbol{n}_f^{(F)}(\phi_{s3},\varphi_{s3},\sigma_{F3})-\boldsymbol{n}_f^{(p)}(\theta_3,u_3,\sigma_{p3})=\boldsymbol{0},\\ \sigma_{p3}=\left(2\pi/N_p\right)(1-\varepsilon),\\ \sigma_{F3}=-\xi+\left(N_p/N_F\right)\left(2\pi/N_p\right)(1-\varepsilon).\end{cases} \quad (51)$$

Because $\left|\boldsymbol{n}_f^{(F)}\right|=\left|\boldsymbol{n}_f^{(p)}\right|=1$, Eqs. (50) and (51) respectively contain six and five independent nonlinear algebraic scalar equations. In other words, Eqs. (50) and (51) form a system of eleven nonlinear equations with eight unknown parameters: θ_1, u_1, θ_3, u_3, ϕ_{s1}, ϕ_{s3}, φ_{s1} and φ_{s3}. The three design

parameters ε_a, ε_b and h_a for the profile L_g of the grinding wheel are added to the eight unknown parameters to form a system of eleven nonlinear equations with eleven unknown parameters as follows:

$$F_i(\theta_1, u_1, \theta_3, u_3, \phi_{s1}, \phi_{s3}, \varphi_{s1}, \varphi_{s3}, \varepsilon_a, \varepsilon_b, h_a) = 0, \quad i = 1, 2, ..., 11 \tag{52}$$

The eleven unknown parameters are determined using Newton's root finding method. The initial guess for the eleven unknown parameters is obtained by solving the following optimization problem:

$$\begin{cases} \min\limits_X Y = \sum\limits_{i=1}^{11} [F_i(X)]^2, \\ X = \{\theta_1, u_1, \theta_3, u_3, \phi_{s1}, \phi_{s3}, \varphi_{s1}, \varphi_{s3}, \varepsilon_a, \varepsilon_b, h_a\}. \end{cases} \tag{53}$$

Solving the optimization problem in Eq. (53) requires the use of a meta-heuristic optimization algorithm. As long as the design parameters ε_a, ε_b and h_a are determined by the system of eleven nonlinear equations, the face gear drive can definitely and precisely produce the predesigned FOFTE.

NUMERICAL EXAMPLES

Example 1

Example 1 verifies that the proposed manufacturing and design method is feasible. Gear module m is set to 10 mm. Pressure angle α is set to 20 degrees. The numbers of teeth on the crowned pinion, the shaper and the face gear are respectively set to 19, 22 and 66. The parameter for the parabolic motion of the grinding wheel, λ, is set to 0.001. The radius of the grinding wheel, ρ_g, is set to 40 mm. The proportion of the left part of the predesigned FOFTE, ε, is set to 0.7. The amplitude of the predesigned FOFTE, ξ, is set to 10 arcsec. In order to produce the predesigned FOFTE, the three design parameters, ε_a, ε_b, and h_a, for the profile L_g of the grinding wheel must be determined using the system of eleven nonlinear equations. A differential evolution algorithm, DE/rand/1/bin, is used to solve the optimization problem in Eq. (53) to obtain the initial guess for the eleven unknown parameters. The solution to the optimization problem is (-8.42472E-4, -6.34222, 4.22764E-3, -9.54734, 1.89304E-1, 1.98516E-1, -6.52967E-2, -7.93193E-2, 0.1, 0.5, 2.82514). The solution is used as the initial guess for the eleven unknown parameters. Using Newton's root finding method to solve the system of eleven nonlinear equations, the results for θ_1, u_1, θ_3, u_3, ϕ_{s1}, ϕ_{s3}, φ_{s1}, φ_{s3}, ε_a, ε_b and h_a are 1.20887E-15, -6.21437, 5.79669E-3, -9.56288, 2.00065E-1, -5.60149E-2, 2.00065E-1, -7.90781E-2, 3.13387E-2, 3.41192E-1 and 2.84076, respectively. Apparently, the three design parameters, ε_a, ε_b and h_a, are also determined. Since all of the parameters for the face gear drive are known, the face gear drive is totally defined so the solid models for the face gear drive are then created, as shown in Figure 9.

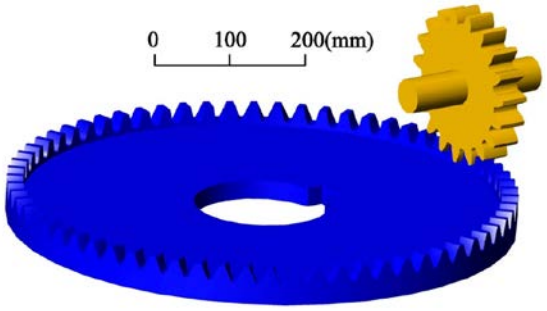

Fig. 9. Solid models for the crowned pinion and the face gear

The actual form of the function of transmission errors is as shown in Figure 10, where SP and EP respectively represent the start point of contact and the end point of contact.

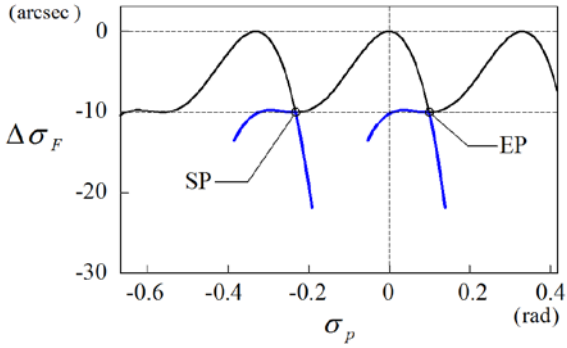

Fig. 10. Actual form of the function of transmission errors

Obviously, the amplitude of the actual form of the function of transmission errors is exactly the same as the predesigned value of 10 arcsec. The shape of the actual form of the function of transmission errors is also exactly the same as that of the predesigned FOFTE. Figures 11 and 12 show the contact paths and the contact ellipses on Σ_p and Σ_F, respectively. The elastic approach δ between Σ_p and Σ_F is set to 0.006 mm (Litvin, 1994). The average for the major axes of the contact ellipses, $\overline{2a}$, is 6.593 mm. The average for the minor axes of the contact ellipses, $\overline{2b}$, is 1.186 mm.

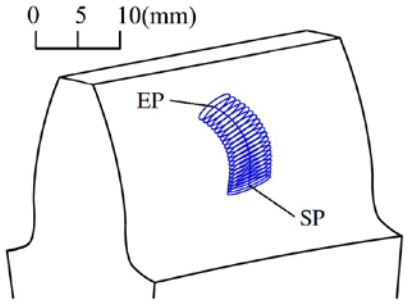

Fig. 11. Contact path and contact ellipses on Σ_p

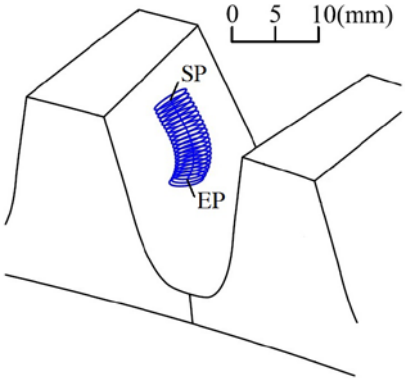

Fig. 12. Contact path and contact ellipses on Σ_F

Example 2

Example 2 shows that $\overline{2a}$ and $\overline{2b}$ can be controlled using parameters λ and ρ_g. Although the explicit forms of $\overline{2a}(\lambda,\rho_g)$ and $\overline{2b}(\lambda,\rho_g)$ are difficult to obtain, the surrogate models $\hat{Y}_{\overline{2a}}(\lambda,\rho_g)$ of $\overline{2a}(\lambda,\rho_g)$ and $\hat{Y}_{\overline{2b}}(\lambda,\rho_g)$ of $\overline{2b}(\lambda,\rho_g)$ are easy to create. A full factorial design of experiment and Kriging interpolation are used to create $\hat{Y}_{\overline{2a}}(\lambda,\rho_g)$ and $\hat{Y}_{\overline{2b}}(\lambda,\rho_g)$. Parameter λ is set to 5 levels: 0.001, 0.002, 0.003, 0.004 and 0.005. Parameter ρ_g is set to 7 levels: 40, 45, 50, 55, 60, 65 and 70. The total number of experiments is 35. For each experiment, the values of $\overline{2a}$ and $\overline{2b}$ are determined using the procedure that is shown in example 1. Table 1 shows the values of $\overline{2a}$ for the 35 experiments. Using Kriging interpolation and the data in Table 1, the Kriging surrogate model $\hat{Y}_{\overline{2a}}(\lambda,\rho_g)$ is developed. The surface plot of $\hat{Y}_{\overline{2a}}(\lambda,\rho_g)$ is as shown in Figure 13.

Table 1. Values of $\overline{2a}$ for the 35 experiments

ρ_g (mm)	$\overline{2a}$ (mm)				
	λ = 0.001	λ = 0.002	λ = 0.003	λ = 0.004	λ = 0.005
40	6.593	5.014	4.081	3.433	2.938
45	6.571	4.968	4.012	3.342	2.824
50	6.549	4.920	3.941	3.247	2.705
55	6.526	4.871	3.867	3.149	2.578
60	6.504	4.821	3.792	3.046	2.444
65	6.481	4.770	3.713	2.938	2.300
70	6.457	4.718	3.633	2.824	2.145

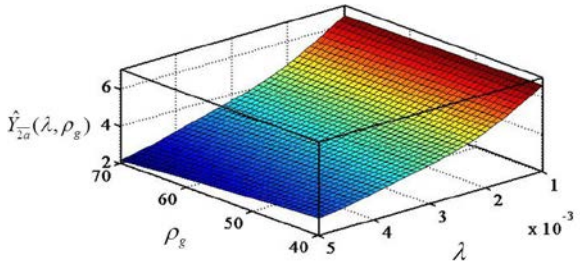

Fig. 13. Surface plot of $\hat{Y}_{\overline{2a}}(\lambda,\rho_g)$ created using Kriging interpolation

Table 2 shows the values of $\overline{2b}$ for the 35 experiments. Using Kriging interpolation and the data in Table 2, the Kriging surrogate model $\hat{Y}_{\overline{2b}}(\lambda,\rho_g)$ is created. The surface plot of $\hat{Y}_{\overline{2b}}(\lambda,\rho_g)$ is as shown in Figure 14.

Table 2. Values of $\overline{2b}$ for the 35 experiments

ρ_g (mm)	$\overline{2b}$ (mm)				
	λ = 0.001	λ = 0.002	λ = 0.003	λ = 0.004	λ = 0.005
40	1.186	1.188	1.187	1.186	1.183
45	1.186	1.188	1.187	1.185	1.182
50	1.186	1.188	1.187	1.185	1.181
55	1.186	1.188	1.187	1.184	1.179
60	1.186	1.188	1.187	1.184	1.178
65	1.186	1.188	1.187	1.183	1.175
70	1.186	1.188	1.186	1.182	1.171

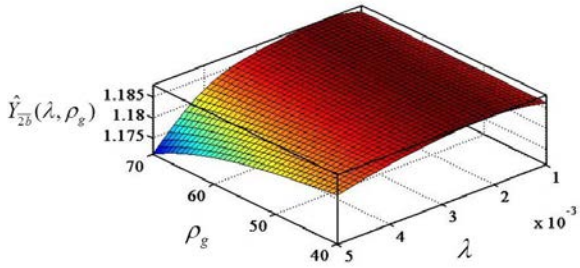

Fig. 14. Surface plot of $\hat{Y}_{\overline{2b}}(\lambda,\rho_g)$ created using

Kriging interpolation

The following optimization model is used to control $\overline{2a}$ and $\overline{2b}$:

$$\max Z = \hat{Y}_{\overline{2b}}(\lambda, \rho_g), \text{ s.t. } \hat{Y}_{\overline{2a}}(\lambda, \rho_g) = L_m. \quad (54)$$

The optimization model in Eq. (54) means to maximize $\hat{Y}_{\overline{2b}}(\lambda, \rho_g)$ subject to the constraint that $\hat{Y}_{\overline{2a}}(\lambda, \rho_g)$ is equal to the controlled value L_m. Three test cases are used to test the accuracy of $\hat{Y}_{\overline{2b}}(\lambda, \rho_g)$ and $\hat{Y}_{\overline{2a}}(\lambda, \rho_g)$. For the first test case, the controlled value L_m is set to 4 mm. For the second test case, the controlled value L_m is set to 5 mm. For the third test case, the controlled value L_m is set to 6 mm. The results for $\hat{Y}_{\overline{2a}}$, $\hat{Y}_{\overline{2b}}$, $\overline{2a}$ and $\overline{2b}$ are shown in Table 3. As the predicted errors are quite small, the surrogate models, $\hat{Y}_{\overline{2a}}(\lambda, \rho_g)$ and $\hat{Y}_{\overline{2b}}(\lambda, \rho_g)$, are sufficiently accurate.

Table 3. Comparison of the predicted and the realistic values for $\overline{2a}$ and $\overline{2b}$

Predicted value	Realistic value	Predicted error
$\hat{Y}_{\overline{2a}}$ (mm)	$\overline{2a}$ (mm)	$\left\|\frac{\hat{Y}_{\overline{2a}} - \overline{2a}}{\overline{2a}}\right\| \times 100\%$
4	4.014184	0.3534%
5	4.99985	0.003%
6	5.91691	1.4043%
$\hat{Y}_{\overline{2b}}$ (mm)	$\overline{2b}$ (mm)	$\left\|\frac{\hat{Y}_{\overline{2b}} - \overline{2b}}{\overline{2b}}\right\| \times 100\%$
1.187267	1.187274	0.00059%
1.187968	1.187962	0.00051%
1.187125	1.187309	0.0155%

CONCLUSIONS

The manufacturing and design method is proposed for the new face gear drive that has a predesigned fourth order function of transmission errors and dimensionally controllable contact ellipses. Numerical example 1 verifies that the new face gear drive can produce the predesigned fourth order function of transmission errors. The bearing contacts are localized in the middle region of the tooth faces. So, there are no edge contact phenomena. Numerical example 2 shows that the optimization model that integrates a full factorial design of experiment and Kriging interpolation can be used to control the average of major axes of the contact ellipses and maximize the average of minor axes of the contact ellipses. The systematic method proposed in this paper can also be applied to develop other new gear drives that have a predesigned FOFTE and dimensionally controllable contact ellipses.

REFERENCES

De Donno, M. and Litvin, F.L., "Computerized design and generation of worm gear drives with stable bearing contact and low transmission errors," *Transactions of the ASME, Journal of Mechanical Design*, Vol. 121, No. 4, pp. 573-578. (1999).

Jiang, J.K. and Fang, Z.D., "Design and analysis of modified cylindrical gear with a higher-order transmission error," *Mechanism and Machine Theory*, Vol. 88, pp. 141-152. (2015).

Litvin, F.L., *Theory of Gearing*, NASA RP-1212, Washington, DC. (1989).

Litvin, F.L., *Gear Geometry and Applied Theory*, Prentice-Hall, Englewood Cliffs, NJ. (1994).

Litvin, F.L. and Lu, J., "Computerized design and generation of double circular-arc helical gears with low transmission errors," *Computer Methods in Applied Mechanics and Engineering*, Vol. 127, No. 1-4, pp. 57-86. (1995).

Litvin, F.L. and Kim, D.H., "Computerized design, generation and simulation of meshing of modified involute spur gears with localized bearing contact and reduced level of transmission errors," *Transactions of the ASME, Journal of Mechanical Design*, Vol. 119, No. 1, pp. 96-100. (1997).

Litvin, F.L., Argentieri, G., De Donno, M. and Hawkins, M., "Computerized design, generation and simulation of meshing and contact of face worm-gear drives," *Computer Methods in Applied Mechanics and Engineering*, Vol. 189, No. 3, pp. 785-801. (2000).

Litvin, F.L., Nava, A., Fan, Q. and Fuentes, A., "New geometry of face worm gear drives with conical and cylindrical worms: generation, simulation of meshing, and stress analysis," *Computer Methods in Applied Mechanics and Engineering*, Vol. 191, No. 27, pp. 3035-3054. (2002a).

Litvin, F.L., Fuentes, A., Zanzi, C. and Pontiggia, M., "Design, generation, and stress analysis of two versions of geometry of face-gear drives," *Mechanism and Machine Theory*, Vol. 37, No. 10, pp. 1179-1211. (2002b).

Lee, C.K. and Chen, C.K., "Mathematical models, meshing analysis and transmission design for a robust cylindrical gear set generated by two blade-discs with parabolic cutting edges," *Proceedings of the Institution of Mechanical*

Engineers, Part C: Journal of Mechanical Engineering Science, Vol. 218, No. 12, pp. 1539-1553. (2004).

Lee, C.K., "Manufacturing process for a cylindrical crown gear drive with a controllable fourth order polynomial function of transmission error," *Journal of Materials Processing Technology*, Vol. 209, No. 1, pp. 3-13. (2009).

Lee, C.K., "A precise and efficient method to manipulate the amplitude of parabolic function of transmission errors," *Advanced Materials Research*, Vol. 1064, pp. 183-190. (2015).

Li, G., Wang, Z.H., Zhu, W.D. and Kubo, A., "A function-oriented active form-grinding method for cylindrical gears based on error sensitivity," *The International Journal of Advanced Manufacturing Technology*, Vol. 92, Issue 5-8, pp. 3019–3031 (2017).

Peng, X.L., Zhang, L. and Fang, Z.D., "Manufacturing process for a face gear drive with local bearing contact and controllable unloaded meshing performance based on ease-off surface modification," *Transactions of the ASME, Journal of Mechanical Design*, Vol. 138, No. 4, pp. 043302. (2016).

Seol, I.H. and Litvin, F.L., "Computerized design, generation and simulation of meshing and contact of worm-gear drives with improved geometry," *Computer Methods in Applied Mechanics and Engineering*, Vol. 138, No. 1-4, pp. 73-103. (1996).

Stadtfeld, H.J. and Gaiser, U., "The ultimate motion graph," *Transactions of the ASME, Journal of Mechanical Design*, Vol. 122, No. 3, pp. 317-322. (2000).

Wang, P.Y. and Fong, Z.H., "Fourth-order kinematic synthesis for face-milling spiral bevel gears with modified radial motion (MRM) correction," *Transactions of the ASME, Journal of Mechanical Design*, Vol. 128, No. 2, pp. 457-467. (2006).

Zanzi, C. and Pedrero, J.I., "Application of modified geometry of face gear drive," *Computer Methods in Applied Mechanics and Engineering*, Vol. 194, No. 27, pp. 3047-3066. (2005).

一種設計方法用於生成具有預設四階傳動誤差函數與尺寸可控制接觸橢圓之新式面齒輪傳動

李政鋼
正修科技大學工業工程與管理系

摘 要

現代齒輪技術已經證實四階傳動誤差函數優於二階傳動誤差函數。四階傳動誤差函數除可降低噪音和振動外，四階傳動誤差函數所組成的運動曲線也比二階傳動誤差函數所組成的運動曲線更為平滑。將二階傳動誤差函數轉換為四階傳動誤差函數已成為最新的研究趨勢。本文提出一種製造與設計方法用於生成具有預設四階傳動誤差函數及尺寸可控制接觸橢圓之新式面齒輪傳動。文中首先應用座標轉換理論、齒輪嚙合原理及微分幾何學建立該面齒輪傳動的齒面位置向量、齒面單位法向量、齒面主曲率與主方向數學模式。接著建立齒面接觸分析與傳動誤差函數斜率之數學模式，並以此模式建立具十一條非線性方程式之非線性聯立方程組，該非線性聯立方程組乃用於迫使該面齒輪傳動具有預設的四階傳動誤差函數。最後應用全因子實驗設計法與克利金插值法來控制接觸橢圓的長軸與短軸平均值。

關鍵字：四階傳動誤差函數、面齒輪、齒面接觸分析、接觸橢圓、主曲率主方向